



UNIVERSITY OF LEEDS

This is a repository copy of *Non-covalent forces tune the electron transfer complex between ferredoxin and sulfite reductase to optimize enzymatic activity.*

White Rose Research Online URL for this paper:
<http://eprints.whiterose.ac.uk/104525/>

Version: Accepted Version

Article:

Kim, JY, Kinoshita, M, Kume, S et al. (9 more authors) (2016) Non-covalent forces tune the electron transfer complex between ferredoxin and sulfite reductase to optimize enzymatic activity. *Biochemical Journal*, 473 (21). pp. 3837-3854. ISSN 0264-6021

<https://doi.org/10.1042/BCJ20160658>

© 2016, The Author(s). Published by Portland Press. This is an author produced version of a paper published in *Biochemical Journal*. Uploaded in accordance with the publisher's self-archiving policy.

Reuse

Unless indicated otherwise, fulltext items are protected by copyright with all rights reserved. The copyright exception in section 29 of the Copyright, Designs and Patents Act 1988 allows the making of a single copy solely for the purpose of non-commercial research or private study within the limits of fair dealing. The publisher or other rights-holder may allow further reproduction and re-use of this version - refer to the White Rose Research Online record for this item. Where records identify the publisher as the copyright holder, users can verify any specific terms of use on the publisher's website.

Takedown

If you consider content in White Rose Research Online to be in breach of UK law, please notify us by emailing eprints@whiterose.ac.uk including the URL of the record and the reason for the withdrawal request.



eprints@whiterose.ac.uk
<https://eprints.whiterose.ac.uk/>

Noncovalent forces tune the electron transfer complex between ferredoxin and sulfite reductase to optimize enzymatic activity

Ju Yaen Kim^{*}, Misaki Kinoshita^{*}, Satoshi Kume^{† ‡}, Guy T. Hanke[§], Toshihiko Sugiki^{*}, John E. Ladbury[¶], Chojiro Kojima^{*}, Takahisa Ikegami[¶], Genji Kurisu^{*}, Yuji Goto^{*}, Toshiharu Hase^{*}, and Young-Ho Lee^{*1}

^{*}Institute for Protein Research, Osaka University, Yamadaoka 3-2, Suita, Osaka 565-0871, Japan

[†] Cellular Function Imaging Team, Division of Bio-function Dynamics Imaging, RIKEN Center for Life Science Technologies, Kobe, Hyogo 650-0047, Japan

[‡] Multi-Modal Microstructure Analysis Unit, RIKEN CLST-JEOL Collaboration Center, 6-7-3 Minatojima-minamimachi, Chuo-ku, Kobe, Hyogo 650-0047, Japan

[§] Department of Plant Physiology, University of Osnabrueck, 11 Barbara Strasse, Osnabrueck 49069, Germany

[¶] School of Molecular and Cellular Biology, University of Leeds, Leeds, UK

[¶] Structural Epigenetics Laboratory, Graduate School of Medical Life Science, Yokohama City University, 1-7-29 Suehiro-cho, Tsurumi-ku, Yokohama 230-0045, Japan

¹To whom correspondence should be addressed: Young-Ho Lee, Institute for Protein Research, Osaka University, Yamadaoka 3-2, Suita, Osaka 565-0871, Japan, Telephone: +81-6-6879-8615; FAX: +81-6-6879-8616; E-mail: mr0505@protein.osaka-u.ac.jp

ABSTRACT

Although electrostatic interactions between negatively-charged ferredoxin (Fd) and positively-charged sulfite reductase (SiR) have been predominantly highlighted to characterize complex formation, the detailed nature of intermolecular forces remains to be fully elucidated.

We herein investigated interprotein forces for formation of an electron-transfer complex between Fd and SiR and their relationship to SiR activity using various approaches over NaCl concentrations between 0 and 400 mM.

Fd-dependent SiR activity assays revealed a bell-shaped activity curve with a maximum around 40-70 mM NaCl and a reverse bell-shaped dependence of interprotein affinity. Meanwhile, intrinsic SiR activity, as measured in a methyl viologen-dependent assay, exhibited saturation above 100 mM NaCl. Thus, two assays suggested that interprotein interaction is crucial in controlling Fd-dependent SiR activity.

Calorimetric analyses showed the monotonic decrease in interprotein affinity on increasing NaCl concentrations, distinguished from a reverse bell-shaped interprotein affinity observed from Fd-dependent SiR activity assay. Furthermore, Fd:SiR complex formation and interprotein affinity were thermodynamically adjusted by both enthalpy and entropy through electrostatic and non-electrostatic interactions. A residue-based NMR investigation on addition of SiR to ¹⁵N-labeled Fd at the various NaCl concentration also demonstrated that a combination of electro- and non-electrostatic forces stabilized the complex with similar interfaces and modulated the binding affinity and mode.

Our findings elucidate that non-electrostatic forces are also essential for the formation and modulation of the Fd:SiR complex. We suggest that a complex configuration

optimized for maximum enzymatic activity near physiological salt conditions is achieved by structural rearrangement through controlled non-covalent interprotein interactions.

SUMMARY STATEMENT

SiR activity assays and ITC/NMR investigation at variable NaCl concentrations reveal that electrostatic and non-electrostatic interactions both stabilize the electron transfer complex between Fd and SiR and optimize the configuration of the complex for higher SiR activity at near-physiological conditions.

SHORT TITLE

Effects of Fd:SiR interactions on SiR activity

KEYWORDS

Electron transfer complex, enzyme activity, ferredoxin, isothermal titration calorimetry, nuclear magnetic resonance, sulfite reductase

ABBREVIATION

ΔG_{bind} , Gibbs free energy for binding; ΔH_{bind} , Change in enthalpy for binding; ΔH_{global} , Change in enthalpy for global unfolding; ΔS_{bind} , Change in entropy for binding; $\Delta C_{\text{p,bind}}$, Change in heat capacity for binding; $\Delta C_{\text{p,global}}$, Change in heat capacity for global unfolding; CSD, Chemical shift difference; CD, Circular dichroism; K_{d} , Dissociation constant; ET, Electron transfer; Fd, Ferredoxin; FNR, Ferredoxin-NADP⁽⁺⁾ reductase; HSQC, Heteronuclear single-quantum coherence correlation; ITC, Isothermal titration calorimetry; T_{m} , Melting temperature; MV, Methyl viologen; K_{m} , Michaelis constant; PCA, Principal component analysis; SiR, Sulfite reductase; k_{cat} , Turnover number.

INTRODUCTION

The physicochemical and structural aspects of the surfaces and active sites of folded proteins are the result of evolution with a high interior packing density and local functional flexibility of proteins [1]. The properties of protein surfaces are a critical factor in ensuring appropriate intermolecular contacts for protein function. A statistical study previously showed that the interfaces of protein-protein complexes consisted of 57% apolar residues, 19% charged residues, and 24% polar residues [2], suggesting that non-covalent interactions, electrostatic and non-electrostatic interactions, are indispensable in interprotein forces.

Non-electrostatic interactions including polar and hydrophobic interactions have been shown to contribute to complex formation of proteins with binding partners. Proteins that accommodate hydrophobic cavities such as GroEL and lipocalin-type prostaglandin D synthase form complexes with hydrophobic molecules [3,4]. The molecular recognition of proline residues of partner proteins by the SH3 domain has also been attributed to non-electrostatic forces [5].

One of the most well-known electrostatic interactions is the attractive charge-charge interaction between positively-charged proteins and the negatively-charged major grooves of DNA [6]. Many studies based on site-directed mutagenesis, electron transfer (ET) rate, X-ray crystallography, and NMR spectroscopy suggested that most redox proteins involved in ET reactions show localized charge clusters on surfaces and utilize predominantly attractive electrostatic interactions among oppositely-charged residues to form an ET complex formation. Positively-charged patches on nitrite reductase [7,8] or [Fe-Fe] hydrogenase [9] interact with negatively-charged surfaces on ferredoxin (Fd). We previously demonstrated that the negative surfaces of Fd also show complementary electrostatic networks with the positively-charged residues of ferredoxin-NADP⁽⁺⁾ reductase (FNR) in the crystal structure of their complex [10].

Disruption in attractive electrostatic interactions by ionic strength or mutation decreased the ET rate and population of the complex [7,9,11-16], clearly indicating the importance of intermolecular electrostatic interactions in forming redox protein complexes.

Meanwhile, distinct patterns of the ET rate between electron-transferring proteins have been observed on changing ionic strength. For instance, while the overall ET rate from cytochrome *c* to plastocyanin decreased monophasically with increasing the salt concentration, that from cytochrome *c* to cytochrome *c* peroxidase or from cytochrome *f* to plastocyanin increased at low salt concentrations and decreased at higher salt concentrations [13,17-19], not simply explained by the electrostatic contribution and complex population. The similar biphasic change was also observed in the electron transfer among *Anabaena* Fd, flavodoxin, FNR, and PSI [20-24]. Interestingly, the change in hydrophobicity on FNR interfaces for Fd or flavodoxin influenced the intermolecular ET rate [22,24]. We have recently revealed that enhancement of interfacial hydrophobicity in Fd increased and decreased activity of FNR and sulfite reductase (SiR), respectively [25].

All these findings raise key questions on the contribution of non-covalent forces such as electrostatic and hydrophobic interactions to formation of ET complexes between oppositely-charged redox proteins and on the relationship between complexation and enzymatic activity under varying conditions such as salt stresses. However, most of studies described the importance of either electrostatic or hydrophobic contribution and no detailed study is available based on various approaches not just ET kinetics.

In this context, we herein selected the enzyme SiR and its physiological electron donor protein Fd as model redox proteins, both of which are derived from the maize leaf. Plant SiR is localized in chloroplasts and catalyzes the reduction of sulfite [26]. SiR plays a key role in the biosynthetic assimilation of sulfur-containing amino acids from inorganic sulfur as well as

in protection against the toxicity associated with the accumulation of sulfite in plant leaves [27]. SiR sequentially receives six electrons from the electron carrier Fd through the repeated formation and dissociation of the Fd:SiR complex, and uses these electrons to reduce sulfite to sulfide. A recent crystallographic analysis showed that SiR consists of 28 helices (218 residues) and 29 strands (106 residues), which correspond to 55% of 583 residues, and the terminal 9-10 residues and a loop of G236-A241 are highly flexible [28]. SiR contains two redox centers, one [4Fe-4S] cluster and one siroheme, for intramolecular electron transfer and catalysis. Four conserved cysteine residues (C494, C500, C540, and C544) for ligating the [4Fe-4S] cluster and siroheme and four conserved residues (R124, R193, K276, and K278), which may be important for substrate recognition, were structurally revealed. SiR showed hydrophobic and hydrophilic surfaces including positively-charged patches.

Our previous study demonstrated the importance of electrostatic interactions between negatively-charged residues on Fd and positively-charged residues on SiR for complex formation and SiR activity [16,26,29]. Mutagenic neutralization of negative charges of Fd on putative interfaces for SiR decreased binding ability of Fd and SiR activity [16,29]. However, non-electrostatic contributions between Fd and SiR to formation of an ET complex and SiR activity are still poorly understood.

We performed in-depth biochemical and biophysical studies on the role of electrostatic and non-electrostatic forces at various NaCl concentrations to control ionic strength and reflect physiological conditions using two types of SiR activity assays, calorimetry for thermodynamic characterization of complex formation, and NMR spectroscopy to examine the binding site and mode at the residue level. We elucidate importance of non-electrostatic interactions and how non-covalent interprotein forces control thermodynamically and mechanically the Fd:SiR complex for SiR activity depending on changes in the NaCl concentration.

MATERIALS AND METHODS

Preparation of proteins

Recombinant SiR from the maize leaf was overexpressed in *Escherichia coli* strain *JM109* cells at 37 °C using Luria-Bertani medium [16]. Cells were grown with vigorous aeration at 37 °C for 3 hours. After decreasing the culture temperature to 27 °C, isopropyl- β -D-thiogalactopyranoside was added at a final concentration of 0.5 mM. Cells were collected by centrifugation at 6,000 rpm for 10 min after further cultivation overnight. They were then suspended in 50 mM Tris-HCl buffer (pH 7.5) containing 150 mM NaCl, 1 mM MgCl₂, 1 mM ethylenediaminetetraacetic acid, and 0.1% β -mercaptoethanol.

After adding phenylmethylsulfonyl fluoride at a final concentration of 0.5 mM, the cell suspensions were disrupted by sonication on ice. The broken cell suspension was centrifuged at 10,000 rpm for 15 min and the supernatant was passed through an anion exchange column (DE-52 resin, GE Healthcare, USA). SiR proteins were recovered from the flow-through fraction and fractionated by salting out with concentrations of ammonium sulfate between 35 and 60%. The precipitated proteins were dialyzed against 25 mM Tris-HCl buffer (pH 7.5) overnight at 4 °C.

The dialyzed proteins were applied to a DEAE-Toyopearl anion exchange column (GE Healthcare, USA) and a chromatographic linear gradient of NaCl developed from 0 to 200 mM in 50 mM Tris-HCl buffer (pH 7.5). The SiR fractions obtained were applied to a phenylsepharose column (GE Healthcare, USA), and eluted with a reverse linear gradient of ammonium sulfate from 40 to 0%.

Recombinant Fds from the maize leaf were overexpressed in *Escherichia coli* strain *JM109* cells and purified as described previously [16,25]. Fd uniformly labeled with ¹⁵N for NMR

measurements were obtained by culturing the bacterial cells in an M9 minimum medium containing $^{15}\text{NH}_4\text{Cl}$ as the sole nitrogen source.

Enzymatic activity assay

Fd- and methyl viologen (MV)-dependent SiR activities were assayed using a reconstituted electron transfer system that resulted in the production of cysteine. The reaction mixture containing Fd (0-40 μM) or MV (1 mM), SiR (200 nM), sodium sulfite (2 mM), O-acetyl serine (10 mM), and cysteine synthase (0.4 U) in 50 mM Tris-HCl buffer (pH 7.5) was prepared at various NaCl concentrations from 0 to 400 mM at 30 °C.

SiR reduction was initiated by an intermolecular electron transfer from Fd, which was reduced by $\text{Na}_2\text{S}_2\text{O}_4$. Reduced SiR sequentially converted sulfite to sulfide. Cysteine synthase, in the presence of O-acetyl serine, produced cysteine from sulfide. The reaction was stopped in 3 min after reducing SiR by the addition of trichloroacetic acid at a final concentration of 20% (volume/volume). The solution was promptly centrifuged at 15,000 rpm for 3 min and 150 μl of the supernatant was collected. After adding 150 μl acetic acid and 150 μl acid-ninhydrin reagent to the supernatant, the solution was heated at 95 °C for 10 min. The further addition of 450 μl ethanol to the solution allowed the production of cysteine to be monitored by increases in absorption intensity at 546 nm.

In order to calculate the Michaelis constant (K_m) and turnover number (k_{cat}), data obtained at the various concentration of Fd (0, 1, 2, 4, 6, 10, 20, and 40 μM) and NaCl (0, 25, 50, 75, 100, 200, 300, and 400 mM) were fit to the Michaelis-Menten equation (equation 1):

$$v = \frac{k_{\text{cat}}[\text{SiR}]_0[\text{Fd}]}{[\text{Fd}] + K_m} \quad \text{Equation 1}$$

where v indicates the initial velocity of the catalytic reaction of SiR, and $[\text{SiR}]_0$ and $[\text{Fd}]$ indicate the concentrations of total SiR and free Fd in the reaction mixture, respectively.

Isothermal titration calorimetry

The isothermal calorimetric titration of Fd to SiR in 50 mM Tris-HCl buffer (pH 7.5) containing NaCl in the range of 0-400 mM (0, 25, 50, 75, 100, and 400 mM) was conducted using a VP-ITC instrument (Malvern, UK) at 30 °C or 25 °C and 27.5 °C at 100 mM NaCl. Binding reactions were initiated by adding Fd (0.85-2 mM) in a syringe to SiR (15-70 μM) in the cell at each NaCl concentration. The titration of Fd comprised 38 injections with a spacing time of 300 s and stirring speed of 307 rpm. The injection volume was 2 or 7 μL for each injection. The corresponding heat of the dilution of Fd titrated to the buffer was used to correct data. Binding isotherms were analyzed with the theoretical curve of equation 2,

$$Q = \frac{n[\text{SiR}]_t \Delta H_{\text{bind}} V_0}{2} \left(1 + \frac{[\text{Fd}]_t}{n[\text{SiR}]_t} + \frac{K_d}{n[\text{SiR}]_t} - \sqrt{\left(1 + \frac{[\text{Fd}]_t}{n[\text{SiR}]_t} + \frac{K_d}{n[\text{SiR}]_t} \right)^2 - \frac{4[\text{Fd}]_t}{n[\text{SiR}]_t}} \right)$$

Equation 2

where Q and n are the total heat content and binding stoichiometry of Fd per SiR, respectively. ΔH_{bind} indicates the change in enthalpy for the binding reaction and V_0 is the volume of the calorimeter cell (~1.43 ml). The total concentrations of SiR and Fd are shown as $[\text{SiR}]_t$ and $[\text{Fd}]_t$, respectively, at any given point during titrations. K_d indicates the dissociation constant, which is the inverse of the association constant (K_a). The values of n , ΔH_{bind} , and K_d were obtained based on a non-linear fit to equation 2. Details of the derivation of equation 2 are provided in Supplementary material.

Changes in Gibbs free energy (ΔG_{bind}) and entropy (ΔS_{bind}) of binding were calculated by using the known values of ΔH_{bind} and K_{d} and the thermodynamic relationships in equation 3 and 4,

$$\Delta G_{\text{bind}} = -RT \ln K_{\text{bind}} = RT \ln K_{\text{d}} \quad \text{Equation 3}$$

$$\Delta G_{\text{bind}} = \Delta H_{\text{bind}} - T\Delta S_{\text{bind}} \quad \text{Equation 4}$$

where R and T are the gas constant and temperature, respectively.

Circular dichroism measurements

Far-UV circular dichroism (CD) measurements of 3 μM (0.2 mg ml^{-1}) SiR were carried out in 50 mM Tris-HCl buffer (pH 7.5) containing NaCl ranging from 0 to 400 mM at 25 °C. Heat scanning of SiR from 20 to 90 °C was also performed by monitoring CD signals at 220 nm at a rate of 1 °C per minute. The apparent melting temperature (T_{m}) was determined by a regression analysis using a nonlinear least squares fitting of data to the sigmoidal equation under the assumption of a two-state transition between folded and unfolded states. It should be noted that we performed thermodynamic analyses although thermal unfolding of SiR was irreversible.

$$\theta_{\text{obs}} = \frac{(a - c) + (b - d)T}{1 + \exp\left(-\frac{\Delta H_{\text{global}}(T_{\text{m}})}{R}\left(\frac{1}{T} - \frac{1}{T_{\text{m}}}\right) + \frac{\Delta C_{\text{p,global}}}{R}\left(\frac{T_{\text{m}}}{T} - 1 + \ln \frac{T}{T_{\text{m}}}\right)\right)} + (c + dT)$$

Equation 5

where θ_{obs} is the signal intensity monitored by CD. The pre- and post-unfolding baselines are described by $a + bT$ and $c + dT$. T , T_m , and R indicate temperature, the midpoint temperature of denaturation, and gas constant, respectively. The change in enthalpy for the global unfolding of SiR is represented by ΔH_{global} and the change in heat capacity is shown by $\Delta C_{p,\text{global}}$. Details of the derivation of equation 5 are available in Supplementary material. CD measurements were performed with a J-720 spectropolarimeter (Jasco, Japan) using a cell with a light path of 1 mm. CD signals between 195 and 250 nm were expressed as the mean residue ellipticity $[\theta]$ ($\text{deg cm}^2 \text{ dmol}^{-1}$). Temperature was regulated using a PTC-423L Peltier-unit (Jasco, Japan).

NMR measurements

A detailed NMR study of SiR in solution remains difficult due to its large size (~65 kDa), which causes severe peak broadening and overlapping. Therefore, solution-state NMR spectroscopy of the ^1H - ^{15}N heteronuclear single-quantum coherence correlation (HSQC) was performed on the smaller ^{15}N uniformly-labeled Fd protein (~10.5 kDa) in the absence and presence of SiR using an AVANCE II-800 spectrometer equipped with a cryogenic probe (Bruker, Germany) in 50 mM Tris-HCl buffer (pH 7.4) containing 10% D₂O at 25 °C.

We selected NaCl concentrations ranging from 0 to 100 mM since the most dynamic changes in SiR activity were observed in this concentration range. In addition, to maximize detection level of NMR peaks, NaCl concentrations above 100 mM were not used, as this decreases sensitivity when using a cryogenic probe. A molar ratio between Fd/SiR of 2:1 was selected, which allowed us to promptly detect NaCl concentration-dependent changes in interprotein affinity, i.e., the population of complexes, (see **RESULTS**) at the residue level by escaping severe peak broadening as would be observed in the presence of excess amounts of SiR. Large molecular weights such as that of the Fd:SiR complex decrease the sensitivity and

resolution of NMR peaks. The protein concentrations for NMR measurements were 100 μM for Fd and 50 μM for SiR. Data were processed by NMRPipe [30] and analyzed by Sparky [31].

Chemical shift differences (CSD) of Fd in the absence and presence of a half molar amount of SiR, here designated finite analysis, were calculated using equation 6:

$$\text{CSD } (\Delta\delta_{\text{ave}}) = ((\Delta\delta_{\text{HN}})^2 + (\Delta\delta_{\text{N}} \times 0.16)^2)^{0.5} \quad \text{Equation 6}$$

where $\Delta\delta_{\text{HN}}$ and $\Delta\delta_{\text{N}}$ are changes in ^1H and ^{15}N chemical shifts in ppm, respectively. The weighting factor of 0.158 was used to adjust the relative magnitudes of the amide nitrogen chemical shift range and the amide proton chemical shift range.

In order to calculate the chemical shift values of Fd, which was saturated by SiR (here designated infinite analysis) we used the relationship in equation 7 [32],

$$\delta_{\text{obs}} - \delta_{\text{free}} = ((\delta_{\text{com}} - \delta_{\text{free}})/[\text{Fd}]_t) ((K_d + [\text{Fd}]_t + [\text{SiR}]_t)/2) - ((\delta_{\text{com}} - \delta_{\text{free}})/[\text{Fd}]_t) (((K_d + [\text{Fd}]_t + [\text{SiR}]_t)^2 - 4[\text{Fd}]_t[\text{SiR}]_t)^{1/2} / 2) \quad \text{Equation 7}$$

where δ_{free} and δ_{obs} indicate the chemical shifts of Fd in the free form and in the presence of SiR, respectively. δ_{com} represents the chemical shifts of Fd in the presence of an infinite amount of SiR. The total concentrations of Fd and SiR are represented by $[\text{Fd}]_t$ and $[\text{SiR}]_t$, respectively.

Principal component analysis of chemical shift perturbation

Principal component analysis (PCA) was performed using the change in chemical shifts obtained from the infinite analysis at each NaCl concentration. The CSD data were represented

as a single-row vector. Then, the vectors were used to build a two-dimensional matrix, in which the rows were the infinite CSD data and the columns were the variables of the NaCl concentration. The matrix size was 78 traceable residues and 5 different NaCl concentrations (0, 25, 50, 75, and 100 mM). The CSD data of each residue were normalized using the mean-centering and variance-scaling. PCA was carried out using the R statistics platform (R Foundation for Statistical Computing, <http://www.r-project.org>). The obtained eigenvalues were expressed as contribution ratios for individual principal components (PC1 and PC2).

RESULTS

NaCl concentration-dependent changes in SiR activity

SiR activity in the range 0-400 mM NaCl was measured with two distinct assays, which differed in the electron donor to SiR: either Fd or MV, i.e., Fd- and MV-dependent SiR activity assays (Figures 1A and B).

SiR activity was first examined using the Fd-dependent assay with a fixed concentration of SiR and Fd (Figure 1A). SiR showed relatively high activity even in the absence of NaCl, and increased in activity with rising NaCl concentrations up to 50 mM. Further elevation of NaCl concentration decreased SiR activity. The activity at 100 mM NaCl was roughly similar to that at 0 mM NaCl. Further increase to higher NaCl concentrations significantly decreased activity. At 400 mM NaCl, 10-fold lower activity than that at 50 mM NaCl was observed. For more detailed information, we performed a fit using a Gaussian function to reveal a NaCl concentration for maximum activity and symmetric dependence of activity to the NaCl concentration. The best-fit result indicated that the NaCl concentration at which SiR has maximum activity is approximately 41 mM (Table 1).

Next, the MV-dependent SiR activity assay was performed at the same NaCl concentrations (Figure 1B). SiR showed appreciable activity at all of the NaCl concentrations examined. By increasing NaCl concentrations from 0 to 400 mM, SiR activity increased progressively and was saturated at approximately 100 mM NaCl. Saturated SiR activity was more than two-fold higher than in the absence of NaCl.

Michaelis-Menten kinetics were investigated by varying the concentration of Fd with a fixed SiR concentration (Figure 1C). Regardless of the NaCl concentration, increased Fd concentrations increased the v value of SiR. However, maximum v increased then decreased with increasing NaCl concentration, as shown in the v_{\max} value (Table 1). The NaCl concentration with the highest v_{\max} was best fit to approximately 63 mM. Similarly, k_{cat} increased with increasing NaCl concentration to 50-75 mM NaCl, while further increase in NaCl resulted in decreased k_{cat} (Figure 1D). Fitting results revealed that k_{cat} was maximal at approximately 66 mM NaCl (Table 1). K_m of SiR for Fd also showed NaCl concentration dependence. The value of K_m decreased from 0 to 100 mM NaCl and increased as NaCl concentrations rose above 100 mM (Figure 1D). A minimum K_m value was best fit to approximately 76 mM NaCl. The catalytic efficiency, k_{cat}/K_m , also showed a similar salt concentration dependent profile to that of v_{\max} and k_{cat} , with a maximum at approximately 63 mM NaCl (Table 1). It should be noted that other fit functions may be used for scattered data in Figure 1A and D.

Thermodynamic investigation of interprotein interactions between Fd and SiR by isothermal titration calorimetry

To obtain information on underlying thermodynamic contribution to binding between Fd and SiR, we carried out an energetic investigation using isothermal titration calorimetry (ITC) at various NaCl concentrations and 30 °C (Figure 2).

During titration of increasing Fd to SiR, exothermic ITC peaks in thermograms, derived from formation of the Fd:SiR complex, were observed at NaCl concentrations between 0 and 100 mM (Figure 2A, upper panels). ITC thermograms at each NaCl concentration except 400 mM showed the decreased magnitude in the negative ITC peaks with consecutive titration of Fd. At the higher molar ratio of Fd to SiR, the ITC peak intensity reached the level of dilution and mixing heat, which indicated the completion of binding reactions. At 400 mM NaCl, the apparent heat of binding was too small to be observed.

Analysis of the ITC thermogram and binding isotherm using the fit and theoretical equations (Figure 2A, lower panels) revealed the underlying thermodynamic parameters for Fd:SiR complex formation: change in enthalpy (ΔH_{bind}), entropy (ΔS_{bind}), and free energy (ΔG_{bind}) as well as the dissociation constant (K_d) with binding stoichiometry (n) (Table 2). The biphasic binding isotherm in the absence of NaCl was best fit by a model with two interacting sites which have different binding affinity, revealing the distinct thermodynamic parameters (Figure 2A, left upper), consistent with our previous study [33].

ΔH_{bind} values obtained at the other NaCl concentrations were all negative and their magnitudes decreased from -4.2 to -0.8 kcal mol⁻¹ with increasing the NaCl concentration (Figure 2B). On the other hand, all ΔS_{bind} values were positive with relatively small differences (-0.7 kcal mol⁻¹) being observed. The binding affinity between Fd and SiR gradually became weaker with increases in the concentration of NaCl because K_d exponentially increased (Figure 1D) and, accordingly, ΔG_{bind} decreased monotonically in magnitude from -8.3 to -6.6 kcal mol⁻¹ (Figure 2B).

Although we cannot exclude the possibility that variation between K_d and K_m was caused by technical differences between ITC and enzyme assays, it is more likely that these differences arise from the fact that K_d values obtained from ITC report all physical binding reactions, including productive and non-productive complex formation, while K_m values obtained from Michaelis-Menten kinetics reflect the affinity of the only productive complex resulting in enzyme activity.

ITC measurements at distinct temperatures (25 and 27.5 °C) were further performed in the presence of 100 mM NaCl (Figure 3). A series of negative ITC peaks representing exothermic reactions were observed at both temperatures (Figures 3A and 3B). Decreasing the temperature from 30 to 27.5 and 25 °C, resulted in slight increases and decreases respectively in the negative values for ΔH_{bind} and $-T\Delta S_{\text{bind}}$ (Figure 3C and Table 2). Thus, the temperature dependence of ΔH_{bind} and $-T\Delta S_{\text{bind}}$ weakened interprotein affinity on decreasing temperature by showing the decrease in the magnitude of ΔG_{bind} from $-6.6 \text{ kcal mol}^{-1}$ at 30 °C to $-6.0 \text{ kcal mol}^{-1}$ at 25 °C.

At all NaCl concentrations and temperatures, except for 0 mM NaCl, the n value was approximately 1, which suggested a 1-to-1 binding stoichiometry between Fd and SiR in solution. However, in the absence of NaCl, the high binding affinity site at a molar ratio ($[\text{Fd}]/[\text{SiR}]$) lower than ~ 2 showed an n value of approximately 1 and the low binding affinity site at higher molar ratios from ~ 2 to ~ 8 indicated an n value of ~ 4 .

Changes in static structures and global dynamics of SiR at various NaCl concentrations examined by far-UV CD spectroscopy

In order to investigate changes in the static and dynamic structures of SiR in the presence of NaCl, far-UV CD measurements were performed at various NaCl concentrations (Figure 4). Static conformations of SiR at the level of secondary structure were first investigated. The

results obtained in the far-UV region without NaCl show the characteristic spectra of a mixture of α -helical and β -strand structures with minima at 210 and 220 nm (Figure 4A). A series of far-UV CD spectra of SiR were obtained at various NaCl concentrations to further characterize the change in the structure of SiR. No change was observed in the pattern of CD spectra, indicating that NaCl does not perturb the secondary structure of SiR.

Sub-global and global dynamics between folded and unfolded conformations without NaCl were examined by observing CD spectra with increasing temperature from 20 to 90 °C (Figures 4B and 4C). The magnitude of whole CD signals decreased with increases in the temperature from approximately 35 °C and were saturated from approximately 70 °C (Figure 4B) indicating cooperative global unfolding (Figure 4C). The CD spectrum at 90 °C exhibited no characteristic profile with low CD intensity even in the presence of NaCl (Figures 4A and 4B), indicating the thermally-unfolded state of SiR. The conformational transition was best fit by a two-state transition model of the global dynamics of SiR, without recognizable sub-global dynamics, producing a melting temperature (T_m) of 55.1 °C and an enthalpy change for global unfolding (ΔH_{global}) of approximately 290 kcal mol⁻¹ (Table 3). The addition of NaCl increased cooperativity of the two-state thermal transition which increased the magnitude of ΔH_{global} (Table 3) and the transition curve was gradually shifted to a higher temperature with increases in the concentration of NaCl (Figure 4C).

Residue-based investigation of NaCl concentration-dependent interprotein interactions by solution-state NMR spectroscopy

Information about weak and strong intermolecular interactions obtained by NMR spectroscopy is extremely useful in evaluating the interacting site and binding mode of proteins in solution, which are otherwise difficult to detect at the residue level [25,34,35].

Sharp NMR signals of ^{15}N -labeled Fd alone were well distributed in ^1H - ^{15}N HSQC spectra at all NaCl concentrations examined, indicating that NaCl does not disturb the structural integrity of native Fd. We then recorded the ^1H - ^{15}N HSQC spectra of ^{15}N -labeled Fd in the presence of SiR at each NaCl concentration. Many Fd peaks were shifted with the addition of SiR at 50 mM NaCl (Figures 5A-5C), which indicates perturbation of electromagnetic environments induced by the formation of a Fd:SiR complex. On decreasing the NaCl concentration from 100 to 0 mM, the degree of peak shifts increased (Figure 5A, inset), which suggests an increase in the population of the Fd:SiR complex.

To obtain detailed quantitative and qualitative information, we calculated the chemical shift difference (CSD) (Figures 5D and 5E) and mapped the residues onto a previously determined crystal structure of Fd (Figure 6) [10]. We used two CSD analyses, finite and infinite analyses (see **MATERIALS AND METHODS**). Since finite analysis provides easy evaluation of the Fd:SiR complex population, it allows identification of key Fd residues for formation of a complex with SiR. On the other hand, infinite analysis allows identification of the accurate binding interface of Fd, which is fully occupied with SiR, thereby revealing subtle differences in the binding modes and relating residues.

Finite analysis showed that both the number of residues with high CSD (over 0.02) and overall CSD values decreased with increasing NaCl concentrations, indicating weakened interprotein affinity. However, despite the decrease in amplitude of CSD, the identity of Fd residues showing CSD were similar (Figure 5D).

Mapping results from finite analysis clarified that many negatively-charged Fd residues were perturbed in the presence of SiR and clustered as expected; however, polar and apolar residues also showed perturbations regardless of the NaCl concentration (Figure 6A). The residues showing greatest CSD were mostly in the three parts of Fd, both terminal parts and

the central part, indicating that these regions of Fd are involved in complex formation with SiR: representatively E11 and E13 in the N-terminal parts, A28, E29, D34, L35, Y37, D60, and Y63 around the [2Fe-2S] cluster, and K91, E92-94, and T96 in the C-terminal part.

Infinite analysis (Figure 5E) and mapping results (Figure 6B) revealed no marked differences in the overall binding interfaces of Fd for SiR over the range of 0 to 100 mM NaCl; however, the relative contributions of each binding region and interacting residue to complex formation and modulation were different. The central regions in the primary sequence of Fd, centered on the [2Fe-2S] cluster, such as A28, E29, G32, D34, L35, Y37, and Y63, generally showed the strongest perturbation, regardless of the NaCl concentration, suggesting that these residues (hereafter called stabilizing residues) were the most fundamental residues for maintaining the complex state. On the other hand, the magnitude of CSD on both terminal parts such as E11 and E13 in the N-terminal part and K91, E92-E94, and T96 in the C-terminal part (designated regulating residues) decreased on increasing the NaCl concentration, indicating distinct binding modes (see **DISCUSSION**).

In order to obtain more information on the change in the binding interface between Fd and SiR depending on the NaCl concentration, principal component analysis (PCA) was performed on the infinite CSD results since PCA is a useful statistical method and reduces a complex dataset to lower dimension to reveal hidden interrelationships among many objects. The two-dimensional PCA plot (PC1 vs. PC2) accounted for 77.1% of total variance (Figure 5F), which indicated a high information content for the PCA plot. PC1 scores at 0, 25, 50, and 100 mM NaCl were clustered on the negative region around -2.5. However, the PC1 score of 75 mM NaCl was approximately 11 and positively contributed to the difference, indicating variance between 75 mM NaCl and all other NaCl concentrations (0, 25, 50, and 100 mM NaCl). On the one hand, the PC2 axis predominantly contained the variance information between either

50 mM or 100 mM NaCl and the other NaCl concentrations (0, 25, and 75 mM). PC2 scores at 0, 25, and 75 mM NaCl were clustered around zero whereas PC2 scores at 50 and 100 mM were around -8 (negative contribution) and 6 (positive contribution), respectively. Thus, the PCA plot reveals NaCl concentration-dependent changes in variance which provide NMR-based information on some differences at the binding interface of Fd and SiR.

DISCUSSION

Interprotein interaction-governed Fd-dependent SiR activity over the intrinsic activity power of SiR

Enzymatic activity is largely controlled by intermolecular interactions between binding partners and the intramolecular catalytic capacity of the enzyme itself. We dissected these two contributions to understand overall activity of SiR by using two types of SiR activity assays: the Fd-dependent assay, which can evaluate the effects of interprotein interactions between the SiR and its physiological electron donor Fd, and the MV-dependent assay, which reflects the intrinsic catalytic capability of SiR since electron transfer to SiR by excessive amounts of MV is not limited by intermolecular interactions.

The shape of electron-transferring rate curves plotted against ionic strength has been used to interpret the degree of control exerted on catalytic rate by interprotein interaction [11,13,17-24]. A bell-shaped curve suggested rearrangement of electron-transfer protein complexes, from an initial complex including the encounter complex to final configuration (i.e., conformational gating for the electron transfer thorough two-step binding), while a monotonically-decreasing curve indicated the absence of the conformational rearrangement of complexes. Thus, a bell-shaped Fd-dependent SiR activity profile over NaCl concentrations (Figures 1A and 1D)

demonstrated that the contribution of interprotein interactions between Fd and SiR to overall SiR activity is considerable.

The impact of SiR structural dynamics on its intrinsic enzymatic capacity at various NaCl concentration was characterized. A saturating curve of SiR activity, obtained by the MV-dependent assay, was consistent with a NaCl concentration dependence of T_m (Figure 4D). This indicated that the increase in the intrinsic activity of SiR may be related to the suppression of global dynamics, possibly due to NaCl-induced molecular compaction without an overall change in secondary structure (Figure 4A), by increasing T_m and the magnitude of negative ΔH_{global} (Table 3).

Comparison of the detailed activity profiles obtained with the two distinct assays further conferred insight into the factors regulating total SiR activity. At 0-100 mM NaCl, while in the Fd-dependent assay SiR exhibited dynamic activity changes, with maximal activity and catalytic efficiency around 40-70 mM NaCl and decreased activity at higher NaCl concentrations, activity in the MV-based assay increased in SiR activity before reaching a plateau (Figure 1B). For example, a higher Fd-dependent SiR activity was measured at 50 mM NaCl than that at 100 mM NaCl despite intrinsic SiR activity at 50 mM NaCl actually being lower than at 100 mM NaCl. Moreover, although MV-based SiR activity retained maximum activity at higher NaCl concentrations over the saturation point of 100 mM NaCl, the Fd-based assay showed minimum activity due to significantly low interprotein affinity (Table 2) resulting from the attenuation of electrostatic interactions.

These findings indicated that maximum SiR activity at moderate concentrations of NaCl is achievable through optimum interactions between Fd and SiR and that intermolecular interaction is a more decisive factor in controlling SiR activity than intrinsic SiR catalytic capacity under physiological conditions (see the final section of **DISCUSSION**).

Intermolecular non-covalent forces thermodynamically control Fd:SiR complex formation

Interprotein interactions are under thermodynamic control, which tends to have a lower ΔG_{bind} by balancing the two driving forces, ΔH_{bind} and $(-T)\Delta S_{\text{bind}}$ [25,36,37]. Therefore, we herein thermodynamically examined complex formation between Fd and SiR using ITC over variable NaCl because ITC reports driving forces which reflect electrostatic and non-electrostatic forces [15,25,36-40], which will be altered as NaCl influences the relative strength of interprotein attraction and interaction. Higher salt concentrations dampen electrostatic and polar interactions, but reinforce hydrophobic interactions.

We performed ITC measurements on addition of Fd to SiR at variable NaCl concentrations, which is a largely-used neutral salt that partly mimics local conditions in cells and chloroplasts [41-43]. Energetically-favourable negative enthalpy changes were observed at all NaCl concentrations (Figures 2A and 2B and Table 2); however, the plot of the driving forces (referred to hereafter as the driving force plot) showed that increasing the amount of NaCl attenuated interprotein affinity by decreasing the magnitude of enthalpy changes (Figure 2C). These results suggest that attractive charge-charge and polar interactions as well as hydrophobic interactions positively contributed to complex formation with enthalpy as a driving force, and that weakened charge and polar interactions due to the disturbance of counter ions or electrostatic screening were compensated by increased hydrophobic interactions.

Consequently, enthalpic gains from electrostatic and polar interactions were dominant over interactions among hydrophobic side chains under higher NaCl concentrations. On the other hand, electrostatic interactions enhance the molecular association rate through long-range electrostatic steering [13,14]; therefore decreased affinity at high salt concentrations accounts

for the decreased association rate (Figure 7), stemming from the attenuation of electrostatic interactions.

As with NaCl concentration, increased temperature is generally followed by decreases and increases in electrostatic and hydrophobic forces, respectively [25]. Thus, the heat capacity change for binding ($\Delta C_{p,bind}$), which is a temperature-dependent enthalpy change ($\Delta C_{p,bind} = \partial\Delta H_{bind}/\partial T$), is also an indicator for the contribution of non-covalent forces to complex formation based on the sign and magnitude of $\Delta C_{p,bind}$ [15,36-38,44]. Most protein complex formation studied by ITC shows a negative $\Delta C_{p,bind}$, indicating that the enthalpic contribution of hydrophobic interactions prevailed over electrostatic and/or polar interactions, even when interactions between oppositely-charged proteins appeared more obvious candidates, such as formation of the Fd:FNR complex ($\Delta C_{p,bind} = -100.4 \text{ cal mol}^{-1} \text{ K}^{-1}$) [37], the putidaredoxin:putidaredoxin reductase complex ($\Delta C_{p,bind} = -296.4 \text{ cal mol}^{-1} \text{ K}^{-1}$) [45], and the P450cam:putidaredoxin complex ($\Delta C_{p,bind} = -308.3 \text{ cal mol}^{-1} \text{ K}^{-1}$) [45]. Therefore, a negative $\Delta C_{p,bind}$ ($-19.7 \text{ cal mol}^{-1} \text{ K}^{-1}$) for formation of the Fd:SiR complex (Figure. 3B and Table 2) also demonstrated contributions from hydrophobic interactions. The small magnitude of $\Delta C_{p,bind}$ in the Fd:SiR complex compared to formation of other ET complexes suggests a large contribution of charge-charge interactions, which increase $\Delta C_{p,bind}$ [15,36,37]. These thermodynamic findings clearly demonstrate that non-electrostatic interactions were also important for Fd:SiR complex formation and that non-covalent forces thermodynamically withstand changes in salt concentration and temperature through energetic adaptation.

Entropy changes also drove complex formation, giving positive values at all NaCl concentrations (Figure 2B), although entropy was not significantly affected by the NaCl concentration as shown in the driving force plot (Figure 2C). This indicates that entropy plays

a key role in stabilizing the Fd:SiR complex as observed in forming the Fd:FNR complex [37] and that enthalpy is a more decisive factor than entropy in controlling interprotein affinity.

Accordingly, the physical binding reactions between oppositely-charged Fd and SiR are favoured by both electrostatic and non-electrostatic interactions. Although other factors, including the behaviour of water, ions, protons, and protein dynamics, probably also contribute, the thermodynamic balance for complex formation between enzymes and electron transfer partners, depending on conditions, can be explained through the general thermodynamic concept of enthalpy-entropy compensation.

Optimization of SiR activity by fine-tuning of the interprotein interaction with Fd under physiological conditions

Stabilizing residues which show high sequence conservation (Figure 8) revealed their importance in forming the Fd:SiR complex. The decrease in the magnitude of CSD of regulating residues correlated well with the decrease in affinity at higher NaCl concentrations. This reveals that the regulating residues play a significant role in determining the interprotein affinity and binding mode. Negatively-charged residues in the C-terminal part were conserved in higher plants and *E. coil*. (Figure 8). Stabilizing and regulating residues, which may be hot spot residues, were both composed of charged and non-charged residues, demonstrating that electrostatic and non-electrostatic interactions were essential for stabilizing complex and adjusting interprotein affinity, in good agreement with the thermodynamic analysis of ITC.

Interestingly, the direction of peak shift for S59 and D60 (Figure 5C) in the presence of SiR varied with NaCl concentration, while the other peaks, such as E92, were shifted to the same direction (Figure 5A, inset). This indicates that a region including S59 and D60 is involved in distinct binding modes depending on the NaCl concentration. Thus, the bell-shaped

activity curve of SiR can be also mechanically explained by a change in the binding mode between Fd and SiR (i.e., structural rearrangement), which was further supported by PCA (Figure 5F).

Taken together, a bell-shaped profile of Fd-dependent SiR activity was demonstrated, based on the affinity and binding mode (Figure 7). At low and moderate NaCl concentrations (approximately 40-70 mM NaCl in 50 mM Tris-HCl buffer), which are close to the physiological conditions in plant chloroplasts (ionic strength of ~0.1-0.15 M) (Figure 7, middle), delicate interprotein regulation optimizes SiR activity by showing a maximum in bell-shaped activity curves. Stabilizing residues form initial complexes, followed by tuning into a productive complex with the best configuration for conformational gating [46] by regulating residues with non-covalent interactions. This fine tuning model rationalizes the discrepancy among the apparently continuous increases in K_d observed in the ITC results, a reverse bell-shaped dependence of the Michaelis constant. At higher NaCl concentrations, e.g., more than several hundred millimolar, (Figure 7, right), collision and diffusion may limit the formation of the stable ET competent complex and decrease the possibility of formation of productive complexes due to geometric constraints of the binding sites [14]. In the absence of NaCl, relatively efficient-complexes can form at the high affinity binding sites on SiR, but also non-productive complex can form at the low affinity binding sites (Table 2), preventing maximum activity (Figure 7, left).

Thus, increasing and decreasing affinity beyond well-controlled interprotein forces may not allow maximum enzymatic activity in terms of kinetics and thermodynamics. Too strong an affinity due to the fast association of reduced Fd and/or the slow dissociation of oxidized Fd in the absence of salts may decrease turnover numbers, and block diffusion from non- or

moderately-productive complex to the best configuration [13,14]. Meanwhile, too weak an affinity is also not adequate for enzymatic function.

Changing physiological electron donor or acceptor proteins to proteins of distinct species or other redox proteins abolishes a bell-shaped ET rate as observed in the Fd:nitrite reductase [7], Fd:FNR [11], and cytochrome *c*:cytochrome *c* peroxidase/plastocyanin systems [18] possibly owing to subtle changes in binding modes. Other physiological factors that may influence enzymatic activity, such as metal-enzyme interactions, temperature, pH, and macromolecular crowding effects are also important for obtaining a deeper understanding of the relationship between physiological conditions and enzyme activity. For example, macromolecular crowding effects not only promote molecular associations, they also suppress global unfolding and molecular diffusion due to the excluded volume effect and steric hindrance [47,48]. Thus, crowding effects in chloroplast may affect the activity curves of SiR at various NaCl concentrations by shifting the bell-shaped activity curve to a lower or higher NaCl concentration and by changing the width of the activity curve. Optimized enzymatic activity near physiological conditions is ensured by the appropriate interplay between the physical, kinetic, and energetic adjustments on complex formation by evolution.

ACKNOWLEDGEMENTS

We thank Prof. Masato Nakai and Prof. Yoko Kimata-Ariga (Osaka University, Japan) for their valuable comments.

FUNDING

This work was supported by Grant-in-Aid for Young Scientists (B) (15K18518 and 25870407) and Grant-in-Aid for Scientific Research (C) (15K07038) for Y.-H. Lee and Platform for Drug Discovery, Informatics, and Structural Life Science from the Ministry of Education, Culture, Sports, Science and Technology, Japan for C. Kojima.

AUTHOR CONTRIBUTION

JYK, TH, and YHL coordinated the study and wrote the paper. JYK prepared all proteins and performed most of the experiments. MK and SK contributed to the CD measurements and the PCA, respectively. All authors analyzed the results and approved the final version of the manuscript.

REFERENCES

- 1 DuBay, K. H., Bowman, G. R. and Geissler, P. L. (2015) Fluctuations within folded proteins: implications for thermodynamic and allosteric regulation. *Acc. Chem. Res.* **48**, 1098-1105
- 2 Wodak, S. J. and Janin, J. (2002) Protein modules and protein-protein interaction. *Advances in Protein Chemistry* **61**, 21-23
- 3 Lin, Z., Schwartz, F. P. and Eisenstein, E. (1995) The hydrophobic nature of GroEL-substrate binding. *J. Biol. Chem.* **270**, 1011-1014
- 4 Kume, S., Lee, Y. H., Nakatsuji, M., Teraoka, Y., Yamaguchi, K., Goto, Y. and Inui, T. (2014) Fine-tuned broad binding capability of human lipocalin-type prostaglandin D synthase for various small lipophilic ligands. *FEBS Lett.* **588**, 962-969
- 5 Kay, B. K., Williamson, M. P. and Sudol, M. (2000) The importance of being proline: the interaction of proline-rich motifs in signaling proteins with their cognate domains. *FASEB J.* **14**, 231-241
- 6 Privalov, P. L., Dragan, A. I., Crane-Robinson, C., Breslauer, K. J., Remeta, D. P. and Minetti, C. A. (2007) What drives proteins into the major or minor grooves of DNA? *J. Mol. Biol.* **365**, 1-9
- 7 Sakakibara, Y., Kimura, H., Iwamura, A., Saitoh, T., Ikegami, T., Kurisu, G. and Hase, T. (2012) A new structural insight into differential interaction of cyanobacterial and plant ferredoxins with nitrite reductase as revealed by NMR and X-ray crystallographic studies. *J. Biochem.* **151**, 483-492
- 8 Srivastava, A. P., Hirasawa, M., Bhalla, M., Chung, J. S., Allen, J. P., Johnson, M. K., Tripathy, J. N., Rubio, L. M., Vaccaro, B., Subramanian, S., et al. (2013) Roles of four

conserved basic amino acids in a ferredoxin-dependent cyanobacterial nitrate reductase. *Biochemistry* **52**, 4343-4353

9 Winkler, M., Kuhlert, S., Hippler, M. and Happe, T. (2009) Characterization of the key step for light-driven hydrogen evolution in green algae. *J. Biol. Chem.* **284**, 36620-36627

10 Kurisu, G., Kusunoki, M., Katoh, E., Yamazaki, T., Teshima, K., Onda, Y., Kimata-Arigo, Y. and Hase, T. (2001) Structure of the electron transfer complex between ferredoxin and ferredoxin-NADP(+) reductase. *Nat. Struct. Biol.* **8**, 117-121

11 Hurley, J. K., Schmeits, J. L., Genzor, C., Gomez-Moreno, C. and Tollin, G. (1996) Charge reversal mutations in a conserved acidic patch in *Anabaena* ferredoxin can attenuate or enhance electron transfer to ferredoxin:NADP⁺ reductase by altering protein/protein orientation within the intermediate complex. *Arch. Biochem. Biophys.* **333**, 243-250

12 Sheinerman, F. B., Norel, R. and Honig, B. (2000) Electrostatic aspects of protein-protein interactions. *Curr. Opin. Struct. Biol.* **10**, 153-159

13 Hope, A. B. (2000) Electron transfers amongst cytochrome *f*, plastocyanin and photosystem I: kinetics and mechanisms. *Biochim. Biophys. Acta.* **1456**, 5-26

14 Schreiber, G. (2002) Kinetic studies of protein-protein interactions. *Curr. Opin. Struct. Biol.* **12**, 41-47

15 Ladbury, J. E. and Williams, M. A. (2004) The extended interface: measuring non-local effects in biomolecular interactions. *Curr. Opin. Struct. Biol.* **14**, 562-569

16 Saitoh, T., Ikegami, T., Nakayama, M., Teshima, K., Akutsu, H. and Hase, T. (2006) NMR study of the electron transfer complex of plant ferredoxin and sulfite reductase: mapping the interaction sites of ferredoxin. *J. Biol. Chem.* **281**, 10482-10488

- 17 Meyer, T. E., Zhao, Z. G., Cusanovich, M. A. and Tollin, G. (1993) Transient kinetics of electron transfer from a variety of c-type cytochromes to plastocyanin. *Biochemistry* **32**, 4552-4559
- 18 Tollin, G., Hurley, J. K., Hazzard, J. T. and Meyer, T. E. (1993) Use of laser flash photolysis time-resolved spectrophotometry to investigate interprotein and intraprotein electron transfer mechanisms. *Biophys. Chem.* **48**, 259-279
- 19 Cruz-Gallardo, I., Diaz-Moreno, I., Diaz-Quintana, A. and De la Rosa, M. A. (2012) The cytochrome *f*-plastocyanin complex as a model to study transient interactions between redox proteins. *FEBS Lett.* **586**, 646-652
- 20 Zhen, Y., Hoganson, C. W., Babcock, G. T. and Ferguson-Miller, S. (1999) Definition of the interaction domain for cytochrome c on cytochrome c oxidase. I. Biochemical, spectral, and kinetic characterization of surface mutants in subunit ii of *Rhodobacter sphaeroides* cytochrome aa(3). *J. Biol. Chem.* **274**, 38032-38041
- 21 Hurley, J. K., Faro, M., Brodie, T. B., Hazzard, J. T., Medina, M., Gomez-Moreno, C. and Tollin, G. (2000) Highly nonproductive complexes with *Anabaena* ferredoxin at low ionic strength are induced by nonconservative amino acid substitutions at Glu139 in *Anabaena* ferredoxin:NADP⁺ reductase. *Biochemistry* **39**, 13695-13702
- 22 Martinez-Julvez, M., Nogues, I., Faro, M., Hurley, J. K., Brodie, T. B., Mayoral, T., Sanz-Aparicio, J., Hermoso, J. A., Stankovich, M. T., Medina, M., et al. (2001) Role of a cluster of hydrophobic residues near the FAD cofactor in *Anabaena* PCC 7119 ferredoxin-NADP⁺ reductase for optimal complex formation and electron transfer to ferredoxin. *J. Biol. Chem.* **276**, 27498-27510
- 23 Nogues, I., Martinez-Julvez, M., Navarro, J. A., Hervas, M., Armenteros, L., de la Rosa, M. A., Brodie, T. B., Hurley, J. K., Tollin, G., Gomez-Moreno, C., et al. (2003) Role of

hydrophobic interactions in the flavodoxin mediated electron transfer from photosystem I to ferredoxin-NADP⁺ reductase in *Anabaena* PCC 7119. *Biochemistry* **42**, 2036-2045

24 Nogues, I., Hervas, M., Peregrina, J. R., Navarro, J. A., de la Rosa, M. A., Gomez-Moreno, C. and Medina, M. (2005) *Anabaena* flavodoxin as an electron carrier from photosystem I to ferredoxin-NADP⁺ reductase. Role of flavodoxin residues in protein-protein interaction and electron transfer. *Biochemistry* **44**, 97-104

25 Kinoshita, M., Kim, J. Y., Kume, S., Sakakibara, Y., Sugiki, T., Kojima, C., Kurisu, G., Ikegami, T., Hase, T., Kimata-Arigo, Y., et al. (2015) Physicochemical nature of interfaces controlling ferredoxin NADP(+) reductase activity through its interprotein interactions with ferredoxin. *Biochim. Biophys. Acta.* **1847**, 1200-1211

26 Nakayama, M., Akashi, T. and Hase, T. (2000) Plant sulfite reductase: molecular structure, catalytic function and interaction with ferredoxin. *J. Inorg. Biochem.* **82**, 27-32

27 Yarmolinsky, D., Brychkova, G., Fluhr, R. and Sagi, M. (2013) Sulfite reductase protects plants against sulfite toxicity. *Plant Physiol.* **161**, 725-743

28 Kim, J. Y., Nakayama, M., Toyota, H., Kurisu, G. and Hase, T. (2016) Structural and mutational studies of an electron transfer complex of maize sulfite reductase and ferredoxin. *J. Biochem.*

29 Akashi, T., Matsumura, T., Ideguchi, T., Iwakiri, K., Kawakatsu, T., Taniguchi, I. and Hase, T. (1999) Comparison of the electrostatic binding sites on the surface of ferredoxin for two ferredoxin-dependent enzymes, ferredoxin-NADP(+) reductase and sulfite reductase. *J. Biol. Chem.* **274**, 29399-29405

30 Delaglio, F., Grzesiek, S., Vuister, G. W., Zhu, G., Pfeifer, J. and Bax, A. (1995) NMRPipe: a multidimensional spectral processing system based on UNIX pipes. *J. Biomol. NMR* **6**, 277-293

- 31 Lee, W., Tonelli, M. and Markley, J. L. (2015) NMRFAM-SPARKY: enhanced software for biomolecular NMR spectroscopy. *Bioinformatics* **31**, 1325-1327
- 32 Akagi, K., Watanabe, J., Hara, M., Kezuka, Y., Chikaishi, E., Yamaguchi, T., Akutsu, H., Nonaka, T., Watanabe, T. and Ikegami, T. (2006) Identification of the substrate interaction region of the chitin-binding domain of *Streptomyces griseus* chitinase C. *J. Biochem.* **139**, 483-493
- 33 Kim, J. Y., Ikegami, T., Goto, Y., Hase, T. and Lee, Y.-H. (2015) Investigation of Protein-Protein Interactions of Ferredoxin and Sulfite Reductase Under Different Sodium Chloride Concentrations by NMR Spectroscopy and Isothermal Titration Calorimetry. In *Molecular Physiology and Ecophysiology of Sulfur* (De Kok, J. L., Hawkesford, J. M., Rennenberg, H., Saito, K. and Schnug, E., eds.), pp. 169-177, Springer International Publishing, Cham
- 34 Mizushima, R., Kim, J. Y., Suetake, I., Tanaka, H., Takai, T., Kamiya, N., Takano, Y., Mishima, Y., Tajima, S., Goto, Y., et al. (2014) NMR characterization of the interaction of the endonuclease domain of MutL with divalent metal ions and ATP. *PLoS One* **9**, e98554
- 35 Bah, A., Vernon, R. M., Siddiqui, Z., Krzeminski, M., Muhandiram, R., Zhao, C., Sonenberg, N., Kay, L. E. and Forman-Kay, J. D. (2015) Folding of an intrinsically disordered protein by phosphorylation as a regulatory switch. *Nature* **519**, 106-109
- 36 Olsson, T. S., Williams, M. A., Pitt, W. R. and Ladbury, J. E. (2008) The thermodynamics of protein-ligand interaction and solvation: insights for ligand design. *J. Mol. Biol.* **384**, 1002-1017
- 37 Lee, Y. H., Ikegami, T., Standley, D. M., Sakurai, K., Hase, T. and Goto, Y. (2011) Binding energetics of ferredoxin-NADP⁺ reductase with ferredoxin and its relation to function. *ChemBiochem* **12**, 2062-2070

- 38 Jelesarov, I. and Bosshard, H. R. (1999) Isothermal titration calorimetry and differential scanning calorimetry as complementary tools to investigate the energetics of biomolecular recognition. *J. Mol. Recognit.* **12**, 3-18
- 39 Velazquez Campoy, A. and Freire, E. (2005) ITC in the post-genomic era...? Priceless. *Biophys. Chem.* **115**, 115-124
- 40 Ladbury, J. E., Klebe, G. and Freire, E. (2010) Adding calorimetric data to decision making in lead discovery: a hot tip. *Nat. Rev. Drug. Discov.* **9**, 23-27
- 41 Robinson, S. P. and Downton, W. J. (1984) Potassium, sodium, and chloride content of isolated intact chloroplasts in relation to ionic compartmentation in leaves. *Arch. Biochem. Biophys.* **228**, 197-206
- 42 Schroppel-Meier, G. and Kaiser, W. M. (1988) Ion homeostasis in chloroplasts under salinity and mineral deficiency : I. Solute concentrations in leaves and chloroplasts from spinach plants under NaCl or NaNO₃ salinity. *Plant Physiol.* **87**, 822-827
- 43 Soriano, G. M., Ponamarev, M. V., Tae, G. S. and Cramer, W. A. (1996) Effect of the interdomain basic region of cytochrome *f* on its redox reactions in vivo. *Biochemistry* **35**, 14590-14598
- 44 Nilapwar, S., Williams, E., Fu, C., Prodromou, C., Pearl, L. H., Williams, M. A. and Ladbury, J. E. (2009) Structural-thermodynamic relationships of interactions in the N-terminal ATP-binding domain of Hsp90. *J. Mol. Biol.* **392**, 923-936
- 45 Aoki, M., Ishimori, K., Fukada, H., Takahashi, K. and Morishima, I. (1998) Isothermal titration calorimetric studies on the associations of putidaredoxin to NADH-putidaredoxin reductase and P450cam. *Biochim. Biophys. Acta.* **1384**, 180-188
- 46 Jeuken, L. J. (2003) Conformational reorganisation in interfacial protein electron transfer. *Biochim. Biophys. Acta.* **1604**, 67-76

- 47 Minton, A. P. (2000) Implications of macromolecular crowding for protein assembly. *Curr. Opin. Struct. Biol.* **10**, 34-39
- 48 Wang, Y., Sarkar, M., Smith, A. E., Krois, A. S. and Pielak, G. J. (2012) Macromolecular crowding and protein stability. *J. Am. Chem. Soc.* **134**, 16614-16618

FIGURE LEGENDS

Figure 1 NaCl-concentration dependent SiR activity monitored by distinct activity assays

(A-C) SiR activity obtained by Fd- (A) and MV-dependent activity assay (B) was plotted against the NaCl concentration. The continuous curves were obtained by fitting to Gaussian (A) and single exponential equations (B) to show symmetric and saturating profiles, respectively. (C) The steady-state kinetics of SiR activity obtained at the various NaCl concentrations were plotted as a function of the concentration of Fd. The continuous lines show the curves fitted based on the Michaelis-Menten equation. The error bars were averaged values of the three independent measurements. (D) K_m in the left axis (red) and k_{cat} in the right axis (blue) respectively were obtained from Michaelis-Menten kinetics and plotted against the concentration of NaCl. The continuous curves were obtained by fitting to the Gaussian equation. K_d values (black) obtained from ITC measurements in the left axis were also plotted. The solid line for K_d is drawn as a visual aid. E , v_{max} in the left axis (red) and k_{cat}/K_m in the right axis (blue) were plotted against the concentration of NaCl, respectively. The continuous curves were obtained by fitting to the Gaussian equation.

Figure 2 Thermodynamic characterization of binding reactions between Fd and SiR using ITC analysis and driving force plot

(A) ITC thermograms of the titration of Fd to SiR at 0, 25, 50, 75, 100, and 400 mM NaCl at 30 °C are shown in the upper panel. Normalized heat values were plotted against the molar ratio ($[Fd]/[SiR]$) in the lower panel. Fitted curves are exhibited using continuous lines. (B and C) The values of ΔH_{bind} (triangle), $-T\Delta S_{bind}$ (rectangle), and ΔG_{bind} (sphere) were plotted as a function of the NaCl concentration (B) and temperature (C). All of the solid lines indicate the

fitting curve with the straight line. **(D)** The driving force plot which describes the change in the driving force (ΔH_{bind} and $-T\Delta S_{\text{bind}}$) and ΔG_{bind} value following complex formation at each NaCl concentration are shown. The dotted diagonal lines with various colors signify the $\Delta\Delta G_{\text{bind}}$ lines of 0 kcal mol⁻¹ for 0 mM NaCl (blue), 1.1 kcal mol⁻¹ for 25 mM NaCl (magenta), 2.1 kcal mol⁻¹ for 50 mM NaCl (green), 2.5 kcal mol⁻¹ for 75 mM NaCl (yellow), and 2.8 kcal mol⁻¹ for 100 mM NaCl (red). Thermodynamically favorable (F) and unfavorable (U) directions following change in NaCl concentration are indicated by blue arrows and red arrows, respectively, outside the panel. The colored arrow in the panel indicates decreases in affinity.

Figure 3 ITC measurements of Fd binding with SiR at distinct temperature

(A and B) ITC thermograms of the titration of Fd to SiR in the presence of 100 mM NaCl at 25 **(A)** and 27.5 °C **(B)** are shown in the upper panel. Normalized heat values were plotted against the molar ratio ($[\text{Fd}]/[\text{SiR}]$) in the lower panel. Fitted curves are exhibited using continuous lines.

Figure 4 Global dynamics of SiR observed by the far-UV CD spectroscopy

(A) The far-UV CD spectra obtained at 20 (solid line) and 90 °C (dotted line) are obtained with increasing NaCl concentrations from 0 to 400 mM. **(B)** The far-UV CD spectra of SiR without NaCl at various temperatures are shown with distinct colors. The increase in temperature from 20 to 90 °C is indicated by the arrow and changing color from magenta to red. **(C)** Thermal scanning of SiR represented by the fraction of folded native SiR using CD intensity at 222 nm is shown. The continuous curves indicate the fitted curve based on the theoretical equation (see **MATERIALS AND METHODS**). The increase in the NaCl concentration was also guided by the arrow. **D**, The melting temperature (T_m) was plotted against the NaCl concentration. The

continuous curve was obtained by fitting to single exponential equations giving a saturating profile.

Figure 5 NMR spectroscopy of ^{15}N -labeled Fd with SiR and chemical shift perturbation analyses

(A) The superposition of ^1H - ^{15}N HSQC spectra of Fd with (blue) and without SiR (red) at 50 mM NaCl is shown. The peak shift of E93 of SiR-bound Fd depending on the NaCl concentration is shown in the inset: 0 (magenta), 25 (cyan), 50 (blue), 75 (yellow), and 100 mM (green). The increasing concentration of NaCl is indicated by the arrow. (B) Magnified central region of the spectra with dramatic perturbations. (C) Peak shifts of D60, which shows variable direction of NMR peak shift of Fd with (blue) and without SiR (red) depending on the concentration of NaCl. The concentration of NaCl is shown and the direction of the peak shift is indicated by black arrows. (D and E) Chemical shift difference (CSD) of Fd in the presence of SiR at 50 mM NaCl calculated by finite (D) and infinite CSD analyses (E) was plotted against the residue number. The secondary structure elements determined from the X-ray structure (PDB/1GAQ) [10] are displayed with labelling in the top part. α -helices (red coils) and β -strands (yellow arrows) are shown. Negatively- and positively-charged residues are represented by red and blue ellipses, respectively. In D stabilizing and regulating regions are also shown with red and green bars, respectively. The red dotted rectangle indicates a putative stabilizing region, which is mostly invisible in NMR spectra due to paramagnetic relaxation enhancement. (F) Two-dimensional plot of principal component analysis (PCA) on the basis of the infinite CSD results obtained at 0 (blue), 25 (magenta), 50 (green), 75 (yellow), and 100 mM NaCl (red) is shown.

Figure 6 Mapping of interacting residues of Fd for SiR onto the crystal structure of Fd (A and B) The degree of the chemical shift difference (CSD) by means of finite (A) and infinite CSD analyses (B) at each NaCl concentration was mapped onto the crystal structure of Fd (PDB ID: 1GAQ) [10]. The color code for the finite CSD analysis is as follows: Red, $CSD > 0.04$; orange, $0.04 > CSD > 0.03$; yellow, $0.03 > CSD > 0.02$. The color code for the infinite CSD analysis is as follows: Pink, $CSD > 0.08$; orange, $0.08 > CSD > 0.06$; yellow, $0.06 > CSD > 0.04$. The NMR invisible peaks (due to paramagnetic relaxation enhancement) are shown by dark gray. Stabilizing and regulating regions are shown with red and green dotted lines, respectively. The stabilizing region includes putative stabilizing residues which are not visible in NMR.

Figure 7 Overall scheme of relations between SiR activity and Fd:SiR interactions depending on variation in salt concentration

Fd-dependent overall (red curve) and intrinsic SiR activity (green curve) are represented. The continuous blue curve indicates trends of the change in interprotein affinity revealed by ITC (K_d). Electron transfer (ET) competent and incompetent Fds are represented by red and deep yellow objects, respectively. SiR is schematically shown in green.

Figure 8 Multiple sequence alignments of Fds

Amino acid sequences of Fds from plant, *E. coli*, and cyanobacterium are compared. The sequences of Fds from maize (ZmFd), spinach (SoFd), *Arabidopsis thaliana* (AtFd), *Synechococcus* PCC7942 (AnFd), and *E. coli* (EcFd) are aligned with gaps inserted to obtain the homology. Color codes are black for conservation and gray for semi-conservation. Asterisks indicate that the residues in that column are identical in all sequences in the alignment.

Table 1 Summary of SiR activity obtained by Michaelis-Menten kinetics

| NaCl (mM) | v_{\max}^a ($\mu\text{M sec}^{-1}$) | k_{cat}^a ($\times 10^4 \text{ sec}^{-1}$) | K_m^a (μM) | k_{cat}/K_m ($\times 10^4 \text{ sec}^{-1} \mu\text{M}^{-1}$) |
|---------------------------------------|--|--|------------------------------|---|
| 0 | 368 ± 5 | 184 ± 2 | 10.4 ± 0.3 | 17.6 ± 0.6 |
| 25 | 390 ± 20 | 190 ± 10 | 4.5 ± 0.8 | 43 ± 8 |
| 50 | 440 ± 10 | 219 ± 7 | 7.4 ± 0.6 | 30 ± 3 |
| 75 | 420 ± 20 | 210 ± 9 | 6.7 ± 0.8 | 32 ± 4 |
| 100 | 390 ± 30 | 200 ± 10 | 6.2 ± 1.3 | 32 ± 7 |
| 200 | 260 ± 10 | 128 ± 5 | 12.6 ± 1.1 | 10 ± 1 |
| 300 | 270 ± 20 | 140 ± 10 | 29.9 ± 3.9 | 4.6 ± 0.7 |
| 400 | 150 ± 20 | 73 ± 8 | 26.7 ± 5.0 | 2.7 ± 0.6 |
| Maximum concentration ^b | 62.5 mM (41.3 mM ^c) | 65.6 mM | 76.1 mM | 62.5 mM |

^a v_{\max} , k_{cat} , and K_m were calculated by fitting the averaged values of the three independent measurements to the equation 1 (see **MATERIALS AND METHODS**).

^bThe NaCl concentration at which a value was maximum with a Gaussian fitting.

^cThe NaCl concentration at which Fd-dependent SiR activity was maximum.

Table 2 Summary of thermodynamic parameters of the Fd:SiR complex formation obtained by ITC

| Temperature | NaCl (mM) | ΔH_{bind} (kcal mol ⁻¹) | $-T\Delta S_{\text{bind}}$ (kcal mol ⁻¹) | ΔG_{bind} (kcal mol ⁻¹) | K_d (μM) | n |
|-------------|--------------|---|---|---|----------------------------|-------------------|
| | 0 | $-4.2 \pm 0.1^{\text{a}}$ | $-5.2 \pm 0.2^{\text{a}}$ | $-9.4 \pm 0.2^{\text{a}}$ | $0.2 \pm 0.1^{\text{a}}$ | 1.0^{a} |
| | | -1.2^{b} | -4.4^{b} | -5.6^{b} | 106^{b} | 4.2^{b} |
| 30 °C | 25 | -3.2 ± 0.1 | -5.1 ± 0.1 | -8.3 ± 0.1 | 1.1 ± 0.1 | 0.9 |
| | 50 | -2.7 ± 0.1 | -4.6 ± 0.1 | -7.3 ± 0.1 | 5.1 ± 0.1 | 0.9 |
| | 75 | -2.3 ± 0.1 | -4.6 ± 0.2 | -6.8 ± 0.2 | 11.8 ± 0.2 | 1.0 |
| | 100 | -0.8 ± 0.2 | -5.8 ± 0.4 | -6.6 ± 0.3 | 17.6 ± 0.2 | 1.0 |
| | 400 | n.d. ^c | n.d. ^c | n.d. ^c | n.d. ^c | n.d. ^c |
| 27.5 °C | 100 | -0.7 ± 0.1 | -5.8 ± 0.2 | -6.5 ± 0.2 | 19.4 ± 0.1 | 1.0 |
| 25 °C | 100 | -0.7 ± 0.0 | -5.4 ± 0.4 | -6.1 ± 0.4 | 42.9 ± 0.0 | 0.9 |

^aThermodynamic parameters for a high affinity binding site. ^bThermodynamic parameters for a low affinity binding site. ^c“n.d.” is shown in cases, in which heat is too small to be detected.

Table 3 Summary of thermodynamic parameters for global dynamics of SiR observed by CD spectroscopy

| NaCl (mM) | T_m^a (°C) | $\Delta H_{\text{global}}^b$ (kcal mol ⁻¹) |
|--------------|-----------------|---|
| 0 | 55.1 ± 0.9 | 70.3 ± 9.1 |
| 10 | 55.3 ± 0.3 | 72.4 ± 7.4 |
| 25 | 56.2 ± 0.7 | 73.1 ± 10.3 |
| 50 | 56.9 ± 1.4 | 75.1 ± 9.6 |
| 75 | 57.1 ± 1.2 | 75.5 ± 9.1 |
| 100 | 56.8 ± 0.5 | 74.6 ± 10.5 |
| 200 | 57.0 ± 0.9 | 75.8 ± 8.8 |
| 300 | 57.5 ± 1.0 | 78.4 ± 7.2 |
| 400 | 57.6 ± 0.6 | 81.3 ± 9.6 |

^aThe averaged value with ^bstandard deviation from two independent measurements are shown.

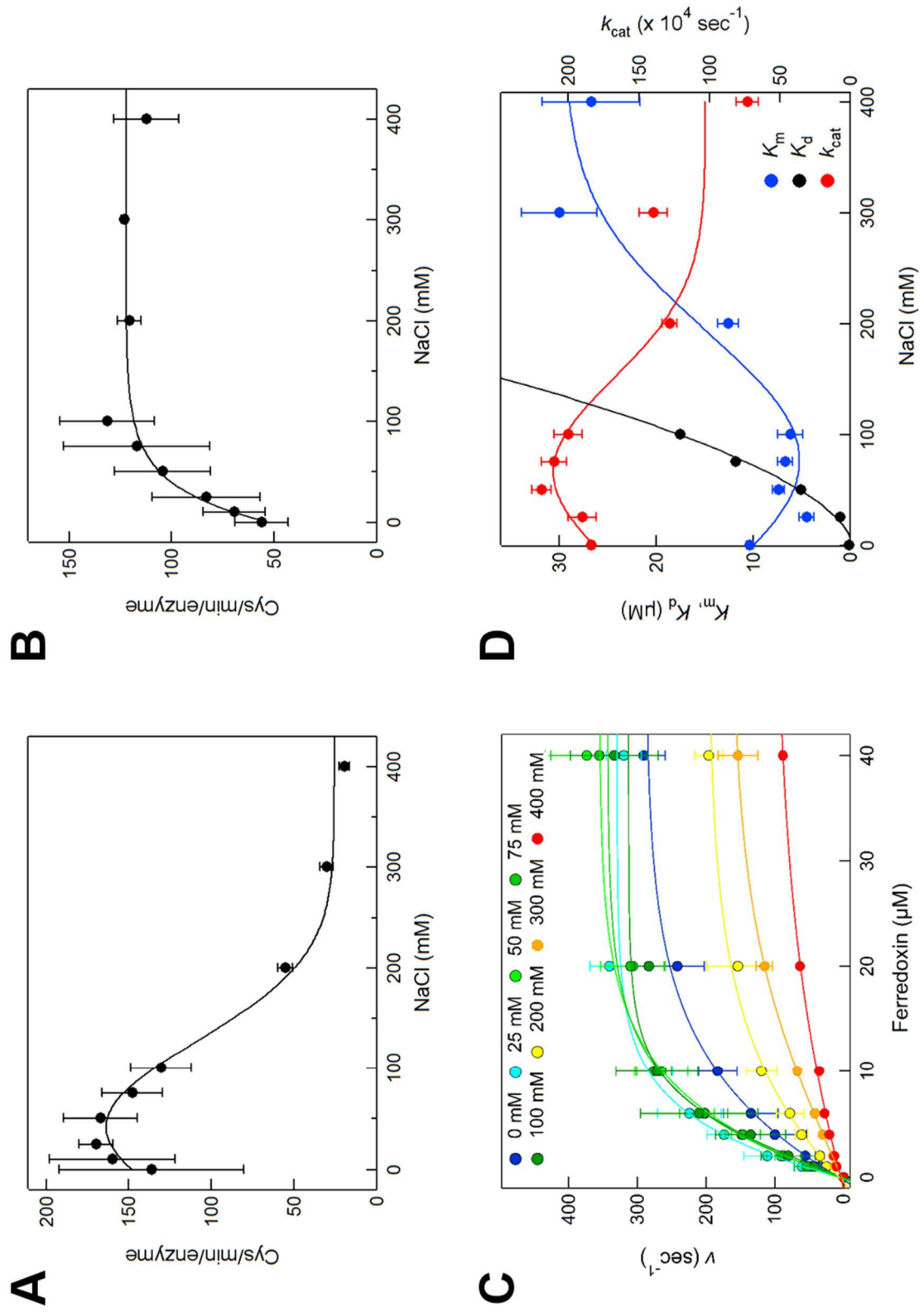


Figure 1

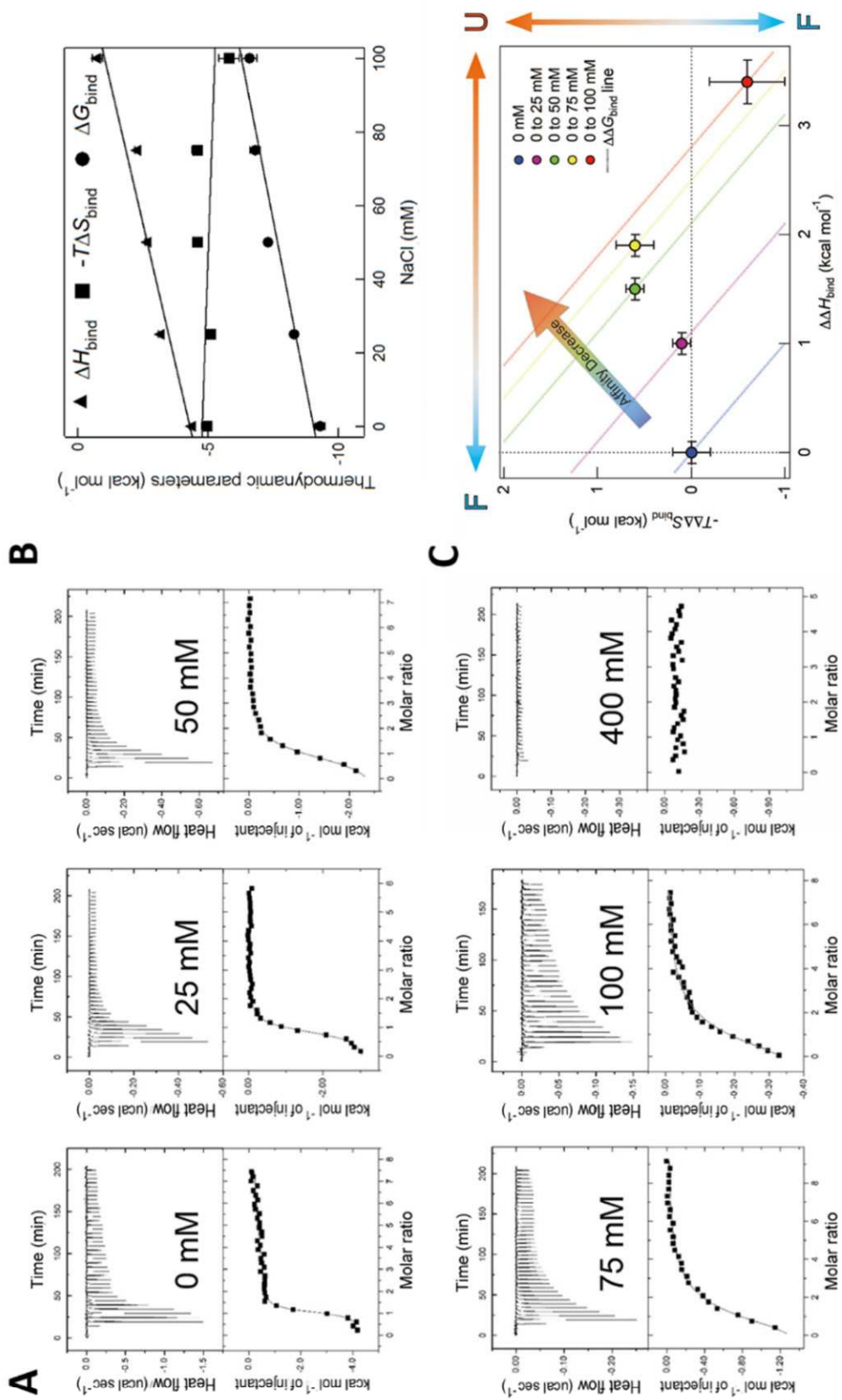


Figure 2

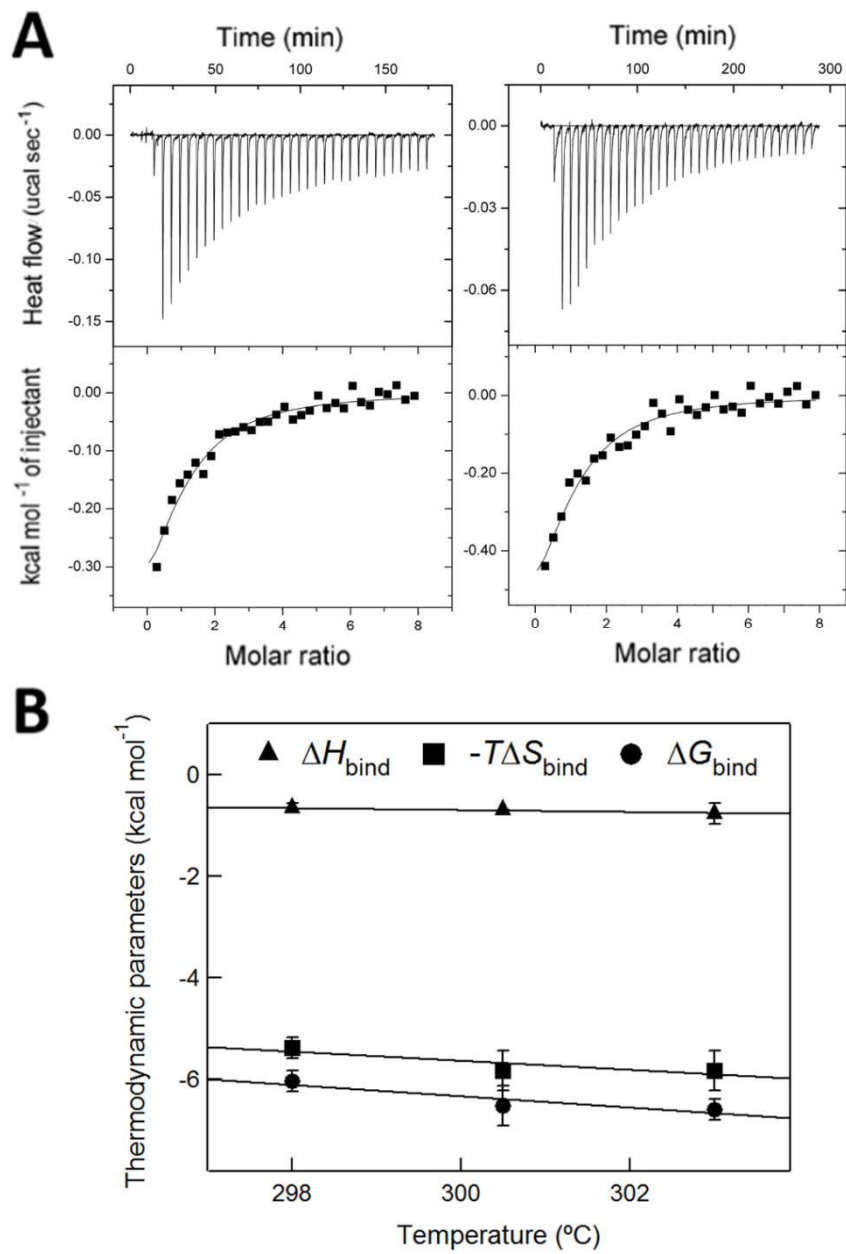


Figure 3

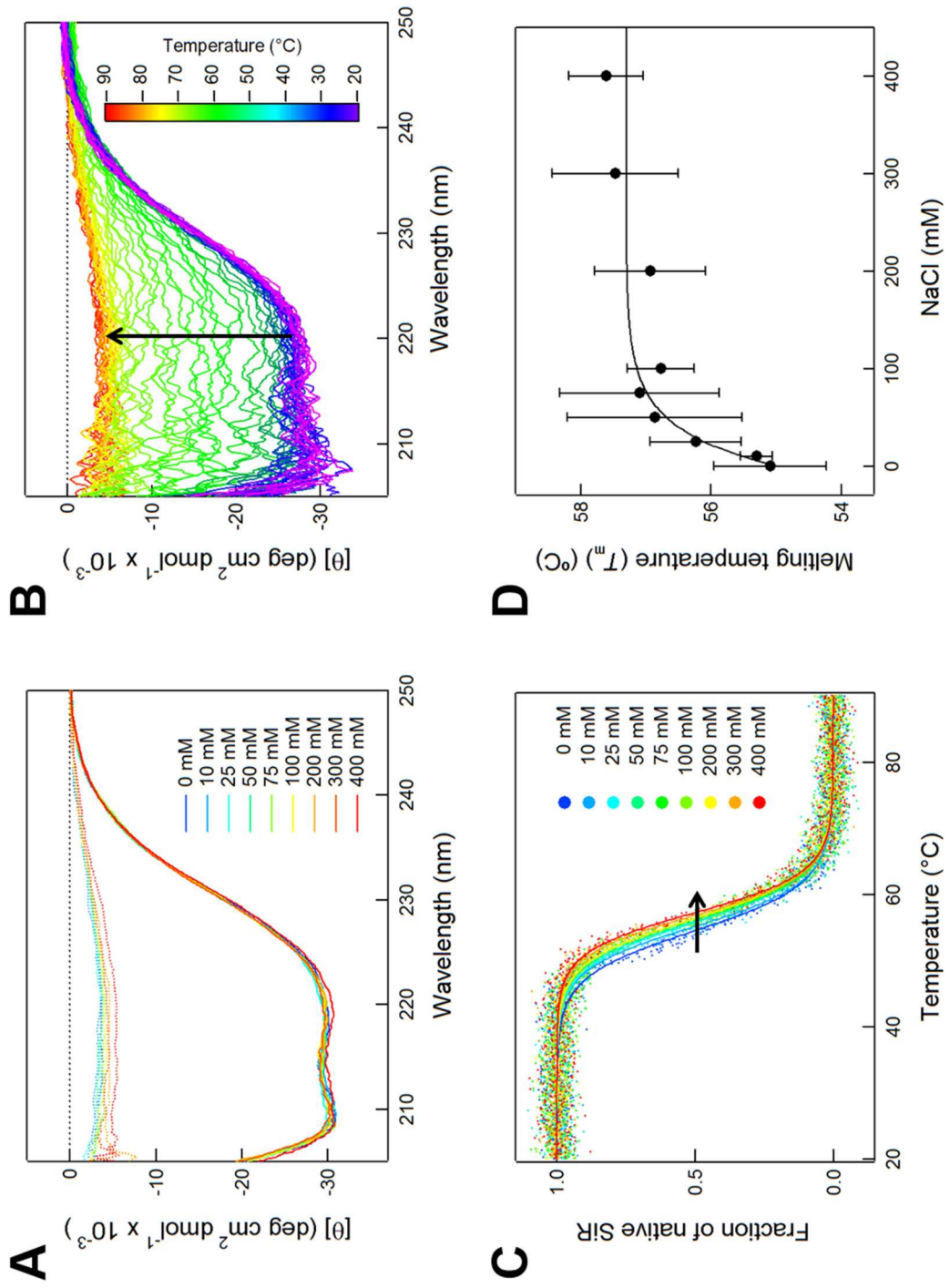


Figure 4

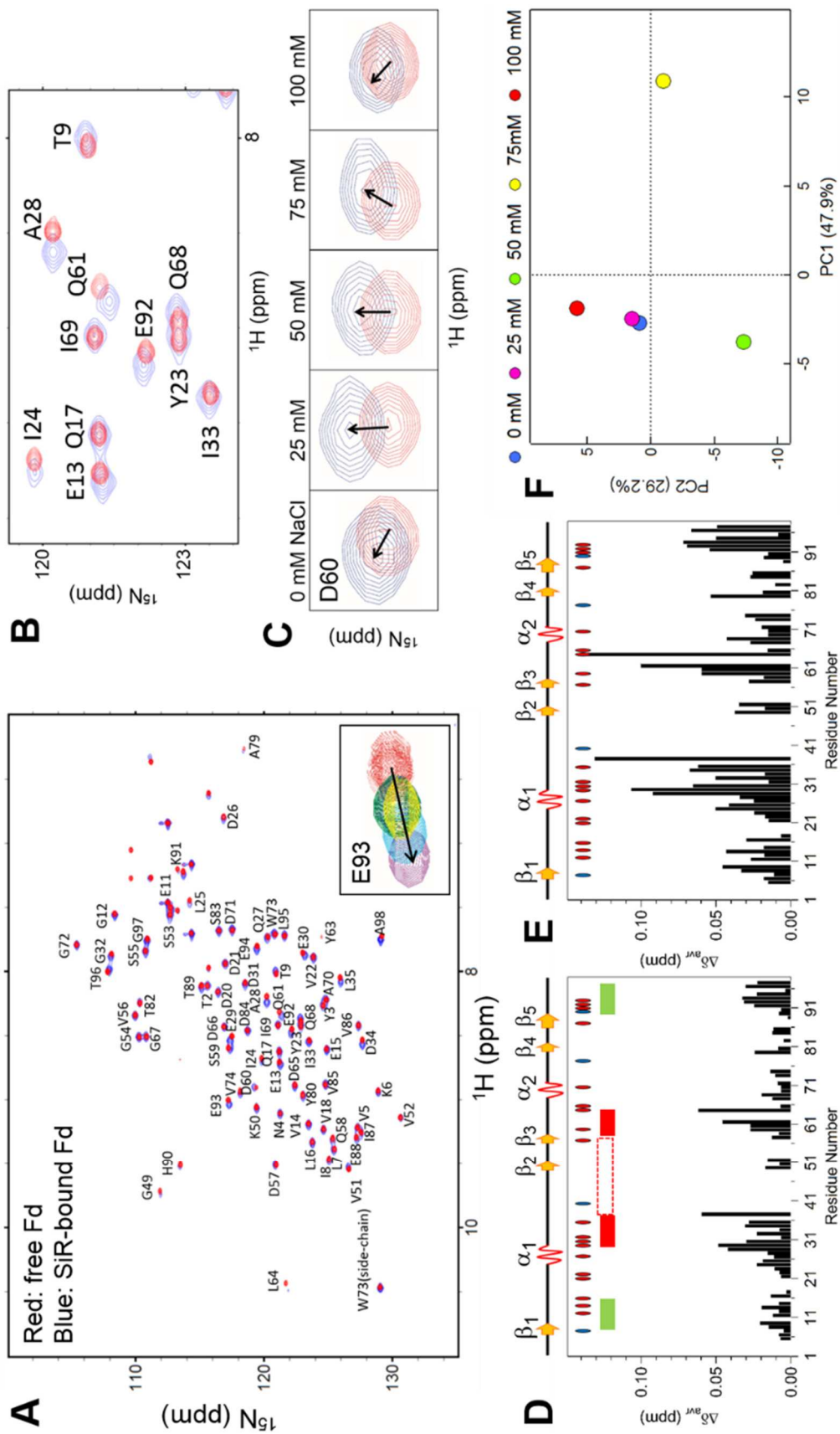


Figure 5

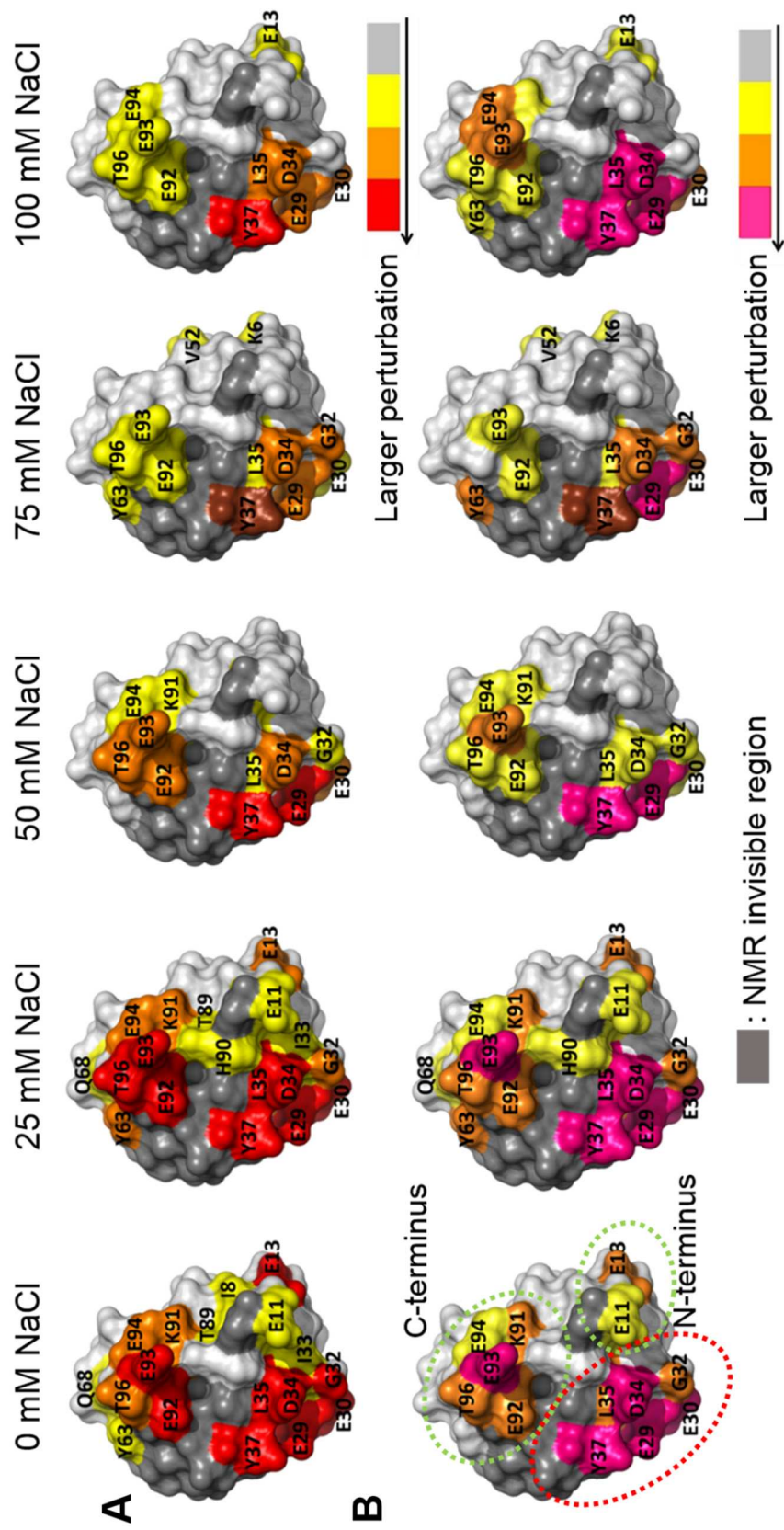


Figure 6

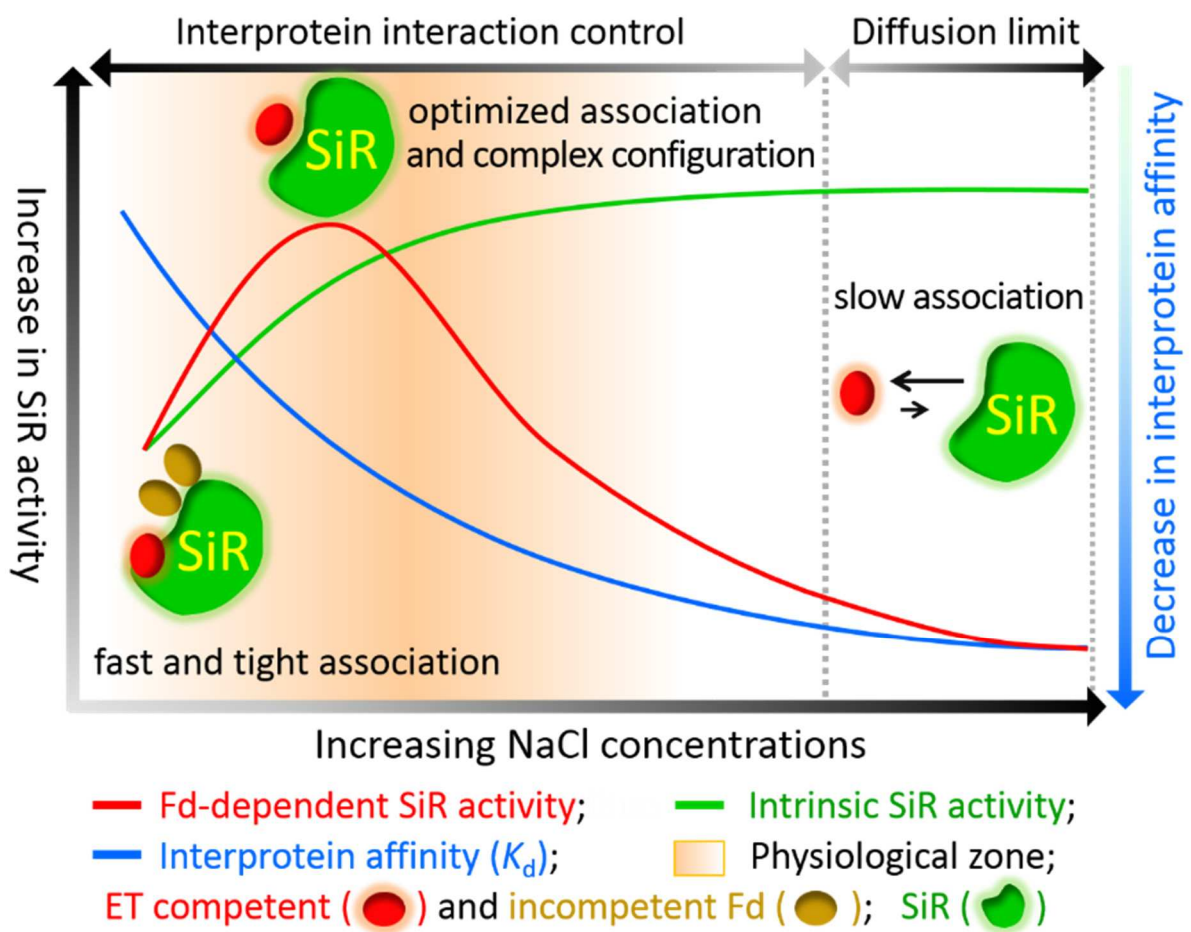


Figure 7

